Nanoscale

PAPER

View Article Online
View Journal | View Issue

Cite this: *Nanoscale*, 2020, **12**, 8563

Polytypism in few-layer gallium selenide†

Soo Yeon Lim, [a] Jae-Ung Lee, [a,b] Jung Hwa Kim,[c,d] Liangbo Liang, [e] Xiangru Kong,[e] Thi Thanh Huong Nguyen,[f] Zonghoon Lee,[c,d] Sunglae Cho[f] and Hyeonsik Cheong *[a]

Received 7th January 2020,
Accepted 8th March 2020

DOI: 10.1039/d0nr00165a

rsc.li/nanoscale

Gallium selenide (GaSe) is one of the layered group-III metal monochalcogenides, which has an indirect bandgap in the monolayer and a direct bandgap in bulk unlike other conventional transition metal dichalcogenides (TMDs) such as MoX_2 and WX_2 (X = S and Se). Four polytypes of bulk GaSe, designated as β-, ε-, γ-, and δ-GaSe, have been reported. Since different polytypes result in different optical and electrical properties even with the same thickness, identifying the polytype is essential in utilizing this material for various optoelectronic applications. We performed polarized Raman measurements on GaSe and found different ultra-low-frequency Raman spectra of inter-layer vibrational modes even with the same thickness due to different stacking sequences of the polytypes. By comparing the ultra-low-frequency Raman spectra with the theoretical calculations and high-resolution electron microscopy measurements, we established the correlation between the ultra-low-frequency Raman spectra and the stacking sequences of trilayer GaSe. We further found that the AB-type stacking is more stable than the AA′-type stacking in GaSe.

1. Introduction

Since the first isolation of graphene in 2004,[1] two-dimensional (2D) layered materials have been studied intensely owing to the possible applications of these materials in future electronics such as flexible devices. Since it is difficult to use pristine graphene in optoelectronic devices due to the lack of a bandgap, semiconducting transition metal dichalcogenides (TMDs) such as MoX_2 and WX_2 (X = S and Se) have attracted much interest and have been studied widely as alternative materials.[2–6] On the other hand, group-III metal monochalcogenides such as GaS, GaSe, and InSe have recently attracted attention as a new family of 2D layered semiconductors since they have high photo-responsivity and external quantum efficiency (EQE) in the UV-range.[7–9] GaSe is one of the group-III metal monochalcogenides, with a direct bandgap energy of ~2 eV in bulk GaSe.[10,11] Additionally, GaSe has been widely used in nonlinear optical applications.[12,13] Group-III metal monochalcogenides have band structures distinct from conventional TMDs. They have a Mexican hat-shaped valence band structure around the Γ-point in momentum space, leading to an indirect bandgap in monolayers.[7,8,14–18] For example, the conduction band minimum of GaSe is at the Γ-point, but the valence band maxima are located slightly away from the Γ-point except for bulk GaSe. However, because of the small energy difference between the valence band maxima and the Γ-point, direct transitions at the Γ-point have a significant effect on the optical properties, resulting in improved optical absorption and emission.[19] Additionally, GaSe is a p-type semiconductor which can be combined with conventional n-type TMDs.[20]

The physical properties of layered materials are sensitive to the thickness and the stacking types in addition to the properties of individual layers. Polytypism is a particular type of polymorphism found in layered materials.[21,22] Even if the structures of the constituent layers are identical, different stacking types between the layers in terms of relative orientations and atomic alignments result in different polytypes.[23] Because many physical properties depend on the polytype, it is important to differentiate the different polytypes in layered materials. In particular, optoelectronic features such as bandgap tunability or valley polarization can be manipulated by controlling the stacking sequence. For example, ABA- and

[a]*Department of Physics, Sogang University, Seoul 04107, Korea. E-mail: hcheong@sogang.ac.kr*
[b]*Department of Physics, Ajou university, Suwon 16499, Korea*
[c]*School of Materials Science and Engineering, Ulsan National Institute of Science and Technology (UNIST), Ulsan 44919, Korea*
[d]*Center for Multidimensional Carbon Materials, Institute for Basic Science (IBS), Ulsan 44919, Korea*
[e]*Center for Nanophase Materials Sciences, Oak Ridge National Laboratory, Oak Ridge, Tennessee 37831, USA*
[f]*Department of Physics and Energy Harvest Storage Research Center, University of Ulsan, Ulsan 44610, Korea*

†Electronic supplementary information (ESI) available. See DOI: 10.1039/d0nr00165a

ABC-stacked trilayer graphene exhibit very different band structures.[24–26] Raman spectroscopy is a widely used method to identify the stacking sequences because it is fast and reliable, and can easily identify polytypes compared to other methods.[27–31] For example, there exist two types of stacking sequences in MoS_2, 3R and 2H, which can be easily identified by using certain low-frequency Raman modes.[32,33]

Monolayer group-III metal monochalcogenides consist of covalently bonded two post transition metal atoms (M) and two chalcogen atoms (X) (X-M-M-X): the monolayer GaSe consists of two Ga atoms sandwiched between two Se atoms as shown in Fig. 1a, whereas its top view shows a hexagonal structure like conventional TMDs. An individual layer of GaSe has the D_{3h} symmetry with four atoms in the unit cell. Bulk GaSe has four different polytypes, designated as β (2H)-, ε (2H′)-, γ (3R)-, and δ (2H-3R)-GaSe as shown in Fig. 1b. Each polytype corresponds to AA′AA′..., ABABAB..., ABCABC... and AA′B′BAA′B′B... stacking sequences, respectively.[34] Position B indicates translation of the top layer A by one-third of a unit cell along the armchair direction of the hexagonal lattice. Position C is an equivalent translation of position B. Positions A′ and B′ denote the mirror images of positions A and B, respectively, with respect to the plane bisecting an armchair bond. All the Ga atoms in one layer are over Se atoms in the successive layer for the AA′ stacking without centered atoms in hexagons, whereas Ga or Se atoms are over the hexagon centers for the AB stacking. δ-GaSe is a mixed type of AA′ and AB stacking (2H and 3R). β-, ε-, γ-, and δ-GaSe have space groups D^4_{6h}, D^1_{3h}, C^5_{3v}, and C^4_{6v} respectively.[33] β-, ε-, and δ-GaSe have hexagonal structures whereas γ-GaSe has a rhombohedral structure. In the bulk phase, the ε-GaSe polytype has been most extensively studied, followed by the γ-GaSe polytype.[35–44] Since the unit cell of δ-GaSe contains four layers, the Brillouin zone of the δ-polytype is smaller than that of the others.[43]

In this work, we carried out polarized Raman spectroscopy of exfoliated few-layer GaSe samples and identified several different Raman spectra for the same thickness. In particular, we identified 4 types of ultra-low-frequency Raman spectra for trilayer GaSe. By comparing high resolution (scanning) transmission electron microscopy (HR-S/TEM) results and theoretical calculations, we establish the correspondence between the Raman spectra and the specific stacking sequences.

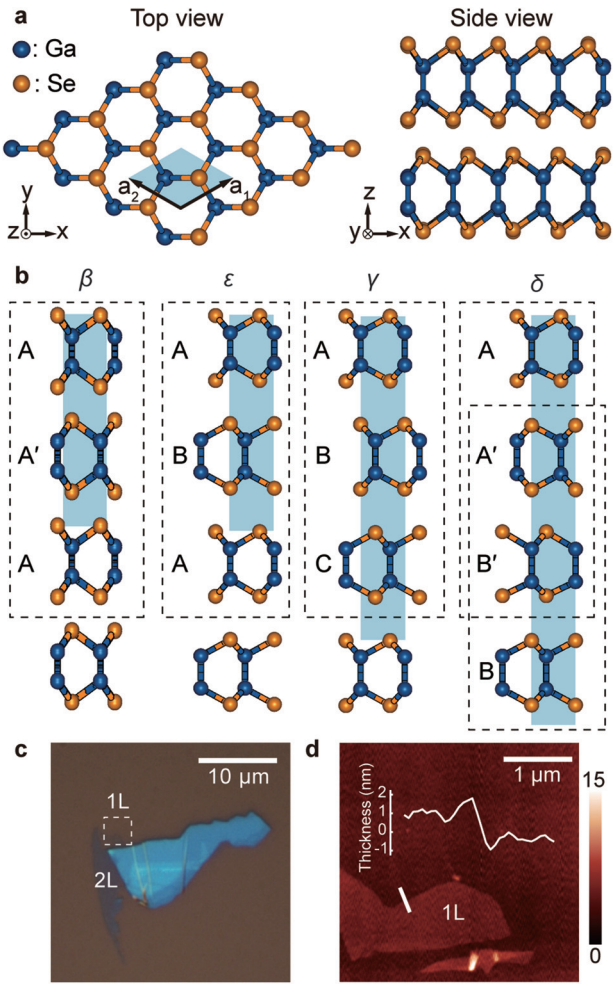

Fig. 1 (a) Top and side view of the GaSe crystal. The unit cell is indicated with a light-blue box. (b) Four different polytypes for bulk GaSe: β-, ε-, γ-, and δ-type. The light-blue boxes are the bulk unit cells for each polytype, and the dashed boxes indicate the stacking sequences of trilayer GaSe. (c) Optical image of a typical GaSe flake on the SiO_2/Si substrate. The white dashed box is the region where AFM measurements were performed. (d) AFM image of the area indicated in (c). The line scan confirms the thickness of the monolayer region.

2. Methods

2.1 Synthesis of GaSe crystal

GaSe single crystals were successfully grown by a temperature gradient method (TGM). Firstly, high purity (99.999%) Ga and Se powders were prepared with a stoichiometric ratio for the growth process, and then loaded into quartz tubes which have a cylindrical shape with a conical bottom. The tubes along with powders were evacuated to an atmosphere of 10^{-4} Torr and sealed using oxygen–hydrogen flame. This tube was inserted into another quartz tube and subsequently sealed under vacuum in order to protect it from ambient air in case the inner tube breaks due to the high vapor pressure of Se during the heating process or due to the difference in the thermal expansion coefficient of GaSe and the quartz tube during the cooling process. The ampules were placed into a vertical furnace and gradually heated to 975 °C, about 15 °C above the melting point of GaSe, and then maintained at that temperature for 16 h for preparing compounds. After this, the molten material was cooled down below the melting point at a very low rate of about 1 °C per hour. The growth process required two weeks to complete and give samples.

2.2 Sample transfer and exfoliation

The samples were fabricated on SiO_2/Si substrates with a 90 nm or 285 nm oxide layer by mechanical exfoliation from GaSe bulk crystals. For TEM measurements, the samples were

exfoliated on polydimethylsiloxane (PDMS) and transferred to graphene on the SiO_2/Si substrate. We placed the samples in a vacuum to avoid degradation from air exposure (see Fig. S1†). The thickness of the sample was confirmed by AFM (NT-MDT).

2.3 Raman measurements

We performed Raman spectroscopy measurements mainly with a diode-pumped solid-state laser with a wavelength of 532 nm (2.33 eV) and a power of ~0.1 mW. In a separate set of measurements, we found that the sample degradation is kept minimal at this excitation power (see Fig. S1†). A 40× objective lens (N.A. = 0.6) was used to focus the laser to a spot of ~1 μm diameter and also collected the scattered light from the sample. The scattered light from the sample was dispersed with a Jobin–Yvon Horiba iHR550 spectrometer (2400 grooves per mm) and was detected with a charge-coupled-device (CCD) using liquid nitrogen for cooling. Reflective volume Bragg gratings (OptiGrate) were used as notch filters to remove the Rayleigh scattered signal, which enables us to observe Stokes and anti-Stokes Raman bands down to 5 cm^{-1}. Polarized Raman measurements were performed with polarizers, $\lambda/4$ waveplates, and $\lambda/2$ waveplates for selecting appropriate polarizations of incident and scattered light.

2.4 TEM measurements

For comparing Raman and TEM results, S/TEM analysis was performed with the particular flakes, characterized by Raman spectroscopy. For S/TEM analysis, exfoliated GaSe flakes on the SiO_2/Si substrate were transferred onto a TEM grid through direct transfer. Because GaSe is significantly oxidized under ambient conditions, the transfer should be completed in short time. Direct transfer has advantages such as reduced transfer time and no formation of poly(methyl methacrylate) (PMMA) residue. Exfoliated GaSe flakes were analyzed using an aberration-corrected FEI Titan cube G2 60-300 with a monochromator. Atomic resolution S/TEM was used for the analysis of the definite stacking order of trilayer GaSe. TEM image simulation was implemented in MacTempasX for interpreting the exact stacking order. All S/TEM analysis was operated at 80 kV.

2.5 Theoretical calculations

Plane-wave density functional theory (DFT) calculations were carried out using the VASP package,[45] with the projector augmented-wave (PAW) method being utilized for electron–ion interactions and local density approximation (LDA) for exchange–correlation interactions. For bulk GaSe, both atomic positions and cell volumes were allowed to relax until the residual forces were below 0.001 eV $Å^{-1}$, where we adopted a k-point sampling of 18 × 18 × 4 in the gamma-centered Monkhorst–Pack scheme[46] with the energy cutoff set at 350 eV. Then, bilayer and trilayer GaSe systems at various stacking configurations were modeled by a periodic slab geometry based on the optimized bulk structure. A vacuum separation of 22 Å in the out-of-plane direction was used to avoid spurious interactions with periodic replicas. For 2D slab calculations, all atoms were relaxed until the residual forces were also below 0.001 eV $Å^{-1}$, with the k-point sampling of 18 × 18 × 1 and the energy cutoff of 350 eV. Subsequently, Raman spectra (both phonon frequencies and Raman intensities) were calculated based on the fully relaxed geometries, by computing the dynamic matrix and derivatives of the dielectric tensors with respect to phonon vibrations.[47,48] Specifically, the dynamic matrix was calculated using an *ab initio* direct method implemented in PHONON software.[49] In the finite difference scheme, the Hellmann–Feynman forces in the 3 × 3 × 1 supercell were computed by VASP for both positive and negative atomic displacements (δ = 0.03 Å), and used in PHONON to construct the dynamic matrix, whose diagonalization provides phonon frequencies and phonon eigenvectors (*i.e.*, vibrations). The derivatives of the dielectric tensor were also calculated by a finite difference approach. For both positive and negative atomic displacements in the single unit cell (δ = 0.03 Å), the dielectric tensors were computed by VASP using density functional perturbation theory and then imported into PHONON to generate their derivatives.[47,48] Finally, Raman intensity of every phonon mode was obtained for a given laser polarization set-up in the typical experimental back scattering configuration to yield Raman spectra after Lorentzian broadening.

3. Results and discussion

The few-layer GaSe samples were prepared by mechanically exfoliating from bulk crystal flakes grown by the temperature gradient method (see the Methods section for details) onto SiO_2/Si substrates with a 90 or 280 nm-thick oxide layer. Fig. 1c and d show the optical image and the corresponding atomic force microscopy (AFM) image of the sample, respectively. The line scan confirmed the thickness of the monolayer sample as shown in Fig. 1d. The monolayer, which is barely resolved in the optical image but can be identified in the AFM image, has a thickness of ~1 nm which is consistent with the inter-layer periodicity of ~0.8 nm from X-ray diffraction measurements.[50,51]

Fig. 2a shows the polarized Raman spectra of monolayer (1L) to five-layer (5L) and bulk GaSe, measured with a 532 nm laser as the excitation source. The stacking sequences of the samples are not identified here. The polarized Raman spectra were obtained in parallel $[\bar{z}(xx)z]$ and cross $[\bar{z}(xy)z]$ polarization configurations. In the parallel polarization configuration, the polarization directions of the incident light and the scattered light are parallel to each other. In the cross polarization configuration, the polarization directions of the incident light and the scattered light are perpendicular to each other. The peaks at ~59, 134, 213, and 308 cm^{-1} correspond to the intra-layer E″, $A'_1(1)$, E′, and $A'_1(2)$ modes of GaSe, respectively, which are similar to the recently reported results.[52] It should be noted that the notations of the vibrational modes depend on the number of layers, but we will use the corresponding notations for bulk ε-GaSe unless otherwise noted. The Raman intensities of the $A'_1(1)$, E′, and $A'_1(2)$ modes measured in the parallel polarization configuration are not dependent on the incident

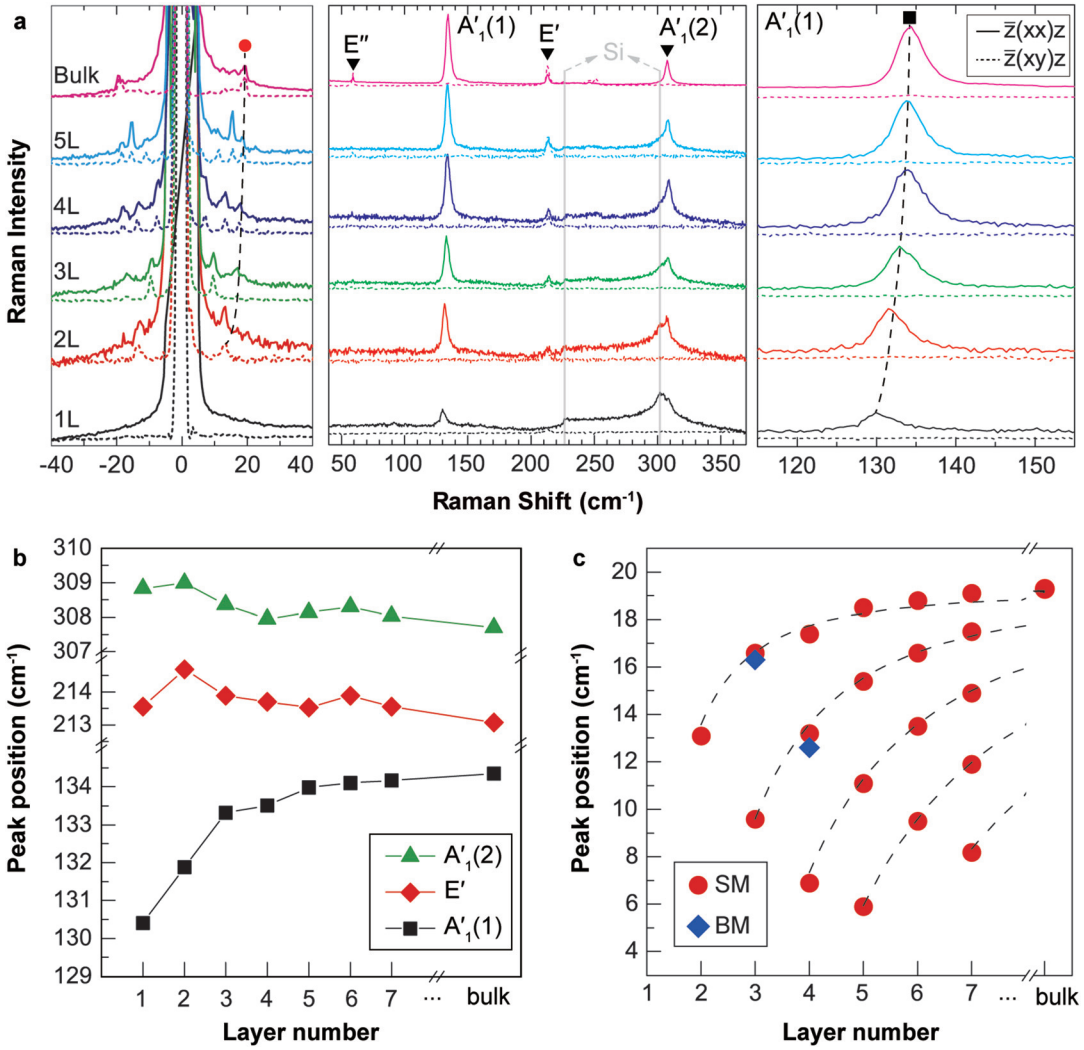

Fig. 2 (a) Representative Raman spectra of GaSe samples from monolayer to bulk measured with a 532 nm (2.33 eV) excitation energy. The solid gray lines indicate the signal from Si substrates. The magnified ultra-low-frequency spectra are shown in Fig. S2.† (b) Thickness dependence of the high-frequency intra-layer vibrational modes: $A'_1(1)$, E′, and $A'_1(2)$. (c) Measured peak positions of the inter-layer shear modes (SM) and the inter-layer breathing modes (BM) as a function of the number of layers. The dashed curves are the best fit to linear chain model calculations.

polarization direction due to the isotropic in-plane symmetry of GaSe (see Fig. S3†). The peak at ~59 cm^{-1} is very weak and can be clearly seen only for thick samples. In addition, weak peaks are occasionally observed at ~245 and 251 cm^{-1} in comparatively thick samples (see Fig. S4†). Their origin is not entirely clear and there are several explanations for them. They could be the E′(LO) mode from ε-GaSe, the $E_{1g}{}^2$ mode from β-GaSe, or the E mode from γ-GaSe.[37–39,41,42,53] On the other hand, our theoretical calculation predicts that a phonon mode corresponding to the bulk Raman inactive A''_2 mode is located near 250 cm^{-1}, and can be Raman activated and appear in few-layer samples due to reduction in symmetry. This is a common phenomenon occurring in other TMDs such as $MoTe_2$.[54] Also, some forbidden modes may appear due to symmetry breaking from crystal imperfections, and even amorphous Se with the Raman peak at ~250 cm^{-1} may exist on the surface since GaSe is easily oxidized.[55–58] Since these peaks are very weak and clearly observed only in relatively thick samples, we will not discuss them further in this work. In the ultra-low-frequency range below 30 cm^{-1}, there are several modes due to the inter-layer shear and breathing vibrations. These are acoustic-like vibrations of the entire layer against each other in the direction parallel to the layer plane (shear) or perpendicular to the layer (breathing).[43,59,60] Because the number of these inter-layer modes and their frequencies depend sensitively on the number of layers, they are the most reliable fingerprints of the number of layers. Furthermore, the inter-layer modes are known to sensitively depend on the stacking sequences in other layered 2D materials such as MoS_2.[31–33,61,62]

Group theory predicts that the in-plane vibrating E modes (including the shear modes) are observed in both the parallel and cross polarization configurations whereas the out-of-plane vibrating A modes (including the breathing modes) are observed only in the parallel polarization configuration (see

Note S1†). Since the breathing modes often overlap with the shear modes, it is difficult to resolve the breathing modes in linearly polarized Raman measurements. However, if one uses circularly polarized light, the breathing modes are allowed only in the same circular polarizations of the incident and scattered photons, whereas the shear modes are allowed only when the circular polarizations of the incident and scattered photons are opposite (see Note S1†).

Fig. 2b shows the peak positions of the three stronger intra-layer modes as a function of the number of layers. Although the higher frequency E′ and $A'_1(2)$ peaks show little variation with the number of layers, the $A'_1(1)$ peak shows a monotonic blueshift with the number of layers which can be used to determine the thickness of thin samples. Fig. 2c shows the positions of the inter-layer vibration modes. The positions of the shear modes were determined from the (linearly) cross-polarization configuration spectra. The breathing modes were determined from the circularly polarized measurements, but their weak intensities prevented us from determining the positions reliably except for a few cases. We, therefore, focus on the shear modes in our analyses below. For each thickness, we measured several samples and found that the shear mode positions vary within experimental uncertainty. Furthermore, although the relative intensities of the shear modes vary for different stacking sequences, the peak positions do not show measurable differences. However, the peak positions of the shear modes show strong variations with the sample thickness (Fig. 2c), a typical behavior for inter-layer vibration modes in 2D layered materials.[63] The dashed curves are fits to the simple linear chain model in which only the layer-to-layer interaction is used as a fitting parameter. The inter-layer force constant thus determined is $\sim(1.33 \pm 0.03) \times 10^{19}$ N m^{-3} along the in-plane direction, which is smaller than those of other typical group VI and VII based TMD layered materials.[60,64–66] Our obtained value is similar to the theoretically estimated values of $\sim 1.20 \times 10^{19}$ N m^{-3} for β-GaSe and $\sim 1.35 \times 10^{19}$ N m^{-3} for ε-GaSe,[67] and our own theoretical estimation of $\sim 1.33 \times 10^{19}$ N m^{-3} for β-GaSe. Therefore, the frequencies of the shear modes shown in Fig. 2c not only allow quick and effective determination of the number of layers in GaSe samples, but also reveal that the inter-layer coupling of GaSe is weaker than that of many common TMDs.

Close inspection of the ultra-low-frequency Raman spectra reveals that the relative intensities of the inter-layer vibration modes vary greatly between samples of the same thickness determined by the positions of the inter-layer vibration modes and the AFM measurements. This indicates that the layers are stacked in different sequences. In order to find the correlation between the Raman spectrum and the stacking sequence, we focused on trilayer GaSe samples. For thicker samples, the number of stacking sequence variations becomes too large for a conclusive analysis. Polarized Raman measurements were performed on multiple points in different flakes (see Fig. S5†). Fig. 3a shows four typical ultra-low-frequency Raman spectra of trilayer samples measured in the cross-polarization configuration. Two shear modes at 9.6 cm^{-1} (S_1) and 16.6 cm^{-1} (S_2) are observed. We assigned four types of ultra-low-frequency spectra in Fig. 3a as: type 1 (black), type 2 (red), type 3 (green) and type 4 (blue). In type 1, the intensity of peak S_1 is higher than that of peak S_2 whereas the intensity ratio is opposite in type 3. In type 2, only peak S_1 appears, and in type 4 only peak S_2 appears. The positions of the two peaks are identical in all four types as mentioned earlier. Fig. 3b shows that the $A'_1(1)$ mode frequency is also identical in all four types, indicating that the intra-layer vibration modes are not affected by the stacking sequences significantly. We examined the positions of the breathing and shear modes separately by using circularly polarized Raman measurements. We observed that the breathing mode does not show much differences in the intensity or the frequency even when the samples have different ultra-low-frequency (shear mode) spectra (see Fig. S6†), which

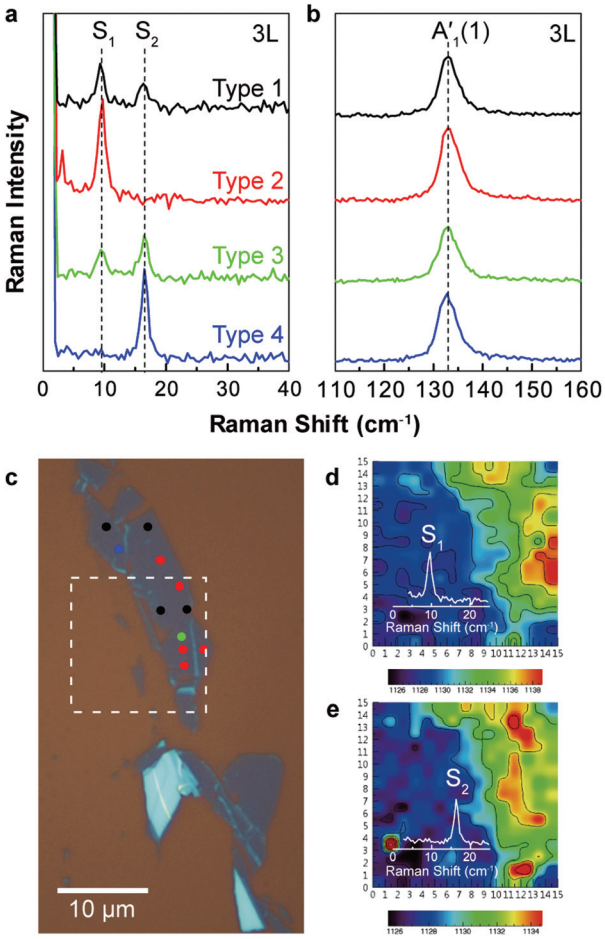

Fig. 3 (a) Four different types of ultra-low-frequency Raman spectra measured in the cross-polarization configuration for trilayer GaSe. (b) The $A'_1(1)$ mode for each stacking sequence measured in the parallel polarization configuration. (c) Optical image of a trilayer GaSe sample where multiple positions were measured. The colored circles indicate the type of the ultra-low-frequency Raman spectrum: black, red, green, and blue circles correspond to the color of the spectra in (a) and (b). (d and e) Raman intensity maps taken from the area indicated by the dashed box in (c), corresponding to peaks (d) S_1 and (e) S_2 in the ultra-low-frequency Raman spectra of (a).

is similar to what has been observed in twisted multilayer graphene.[68,69]

Furthermore, we investigated several trilayer flakes which show a distribution of different ultra-low-frequency spectra. Fig. 3c shows an optical microscope image of one such sample, with the measurement point marked. The colors of the points match the spectrum type shown in Fig. 3a. Fig. 3d and e show the Raman intensity images of peaks S_1 and S_2 obtained from the area indicated by the dashed box in Fig. 3c, respectively. The distribution of the peak intensities matches the spectrum types as shown in Fig. 3c, clearly showing a distribution of areas with different ultra-low-frequency Raman spectra. This result implies that GaSe exists in different areas of stacking sequences even in the same thickness flake. We also found that some flakes comprise mostly only one type (see Fig. S5e† and Fig. 1). We found more flakes having various stacking sequences than flakes having only one stacking sequence, although type 2 and type 4 were relatively more frequently found.

In order to correlate the Raman spectra and the stacking sequences, we theoretically calculated ultra-low-frequency Raman spectra for possible stacking sequences of trilayer GaSe. Fig. 4a shows the four different ultra-low-frequency Raman spectra calculated *via* first-principles density functional theory (DFT) according to the procedure explained in the Methods section. The calculated non-resonant Raman intensities of low-frequency S_1 and S_2 peaks vary considerably with the stacking sequences, similar to the experimental trends shown in Fig. 3a. In contrast, Fig. 4b shows that the high-frequency intra-layer modes are virtually identical in all stacking sequences, which is reasonable because the intra-layer modes are less sensitive to stacking changes than the inter-layer modes.

In addition to the DFT method above, the Raman intensities of low-frequency inter-layer modes in 2D materials can also be computed by a simple inter-layer bond polarizability model proposed in our previous work.[70] This model can provide more physical insights compared to the DFT approach. Generally speaking, the Raman intensity of each normal mode is proportional to the change in the system's polarizability with respect to the normal coordinates of the corresponding vibration, and so obtaining the polarizability change by the vibration is crucial for calculating the intensity. For an inter-layer vibration mode, each layer oscillates as a quasi-rigid body, and therefore it can be treated as a single object. For layer i, if the derivative of the system polarizability with respect to its displacement is α'_i and its displacement during the inter-layer vibration is Δr_i, the change in the polarizability by this displacement is $\Delta\alpha_i = \alpha'_i \cdot \Delta r_i$. The total change in the system polarizability by the inter-layer vibration is the sum of the changes in every layer: $\Delta\alpha = \sum_i \Delta\alpha_i = \sum_i \alpha'_i \cdot \Delta r_i$, where α'_i is related to the properties of the inter-layer bonds, including the inter-layer bond polarizabilities and the inter-layer bond vectors (lengths and directions).[70] The general form of α'_i can be simply determined based on the directions of the inter-

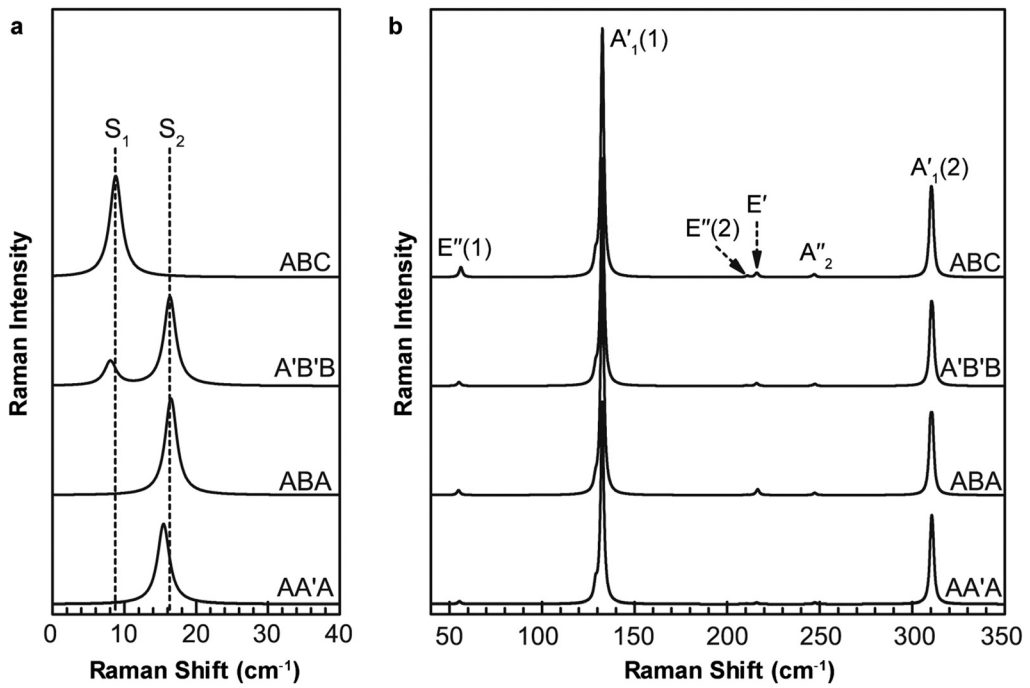

Fig. 4 Calculated non-resonant Raman spectra of trilayer GaSe with respect to different stacking sequences based on DFT. (a) Ultra-low-frequency Raman spectra of trilayer GaSe which show inter-layer shear modes S_1 and S_2. Note that the S_1 peak intensity in A'B'B stacking was increased by one order of magnitude for better display. (b) High-frequency Raman spectra which show intra-layer vibrational modes E''(1), A'_1(1), E''(2), E', A''_2 and A'_1(2), following the bulk symmetry notations.

layer bond vectors.[63,70] Meanwhile, the displacement of each layer, Δr_i, can be determined by the linear chain model.[65] Finally, the Raman intensity of the inter-layer vibration mode is obtained based on the formula $I \propto \frac{n+1}{\omega}|\Delta\alpha|^2$, where $n = \left(e^{\frac{\hbar\omega}{k_B T}} - 1\right)^{-1}$ is the phonon occupation according to Bose–Einstein statistics and ω is the frequency of the vibration mode.

In trilayer GaSe, for an inter-layer shear vibration along the x direction, the polarizability change is $\Delta\alpha = \sum_i \alpha'_i \cdot \Delta x_i$, where α'_i can change notably with the stacking, since it is sensitive to the inter-layer bond polarizabilities and bond directions that vary with the stacking, according to the inter-layer bond polarizability model.[63,70] Similar to bilayer MoS_2,[63] bilayer GaSe has two stacking patterns of AA′ and AB, and the inter-layer bond properties are different as the relative layer-to-layer atomic alignments are different between AA′ and AB stackings. This is confirmed by the reported different low frequency Raman intensities of bilayer $MoSe_2$ and MoS_2 in these two stacking sequences.[32,33,71] For trilayer GaSe, there are a variety of stacking sequences, including AA′A, ABA, ABC, AA′B′, and A′B′B, as shown in Fig. 1b and Fig. S7.† Note that both AA′B′ and A′B′B originate from the bulk stacking AA′B′B in Fig. 1b, and A′B′B is equivalent to ABB′, where BB′ is equivalent to AA′. For AA′A stacking in trilayer GaSe, the top layer and bottom layer (*i.e.*, layer 1 and layer 3) are in the equivalent positions, thereby giving $\alpha'_1 = \alpha'_3 = \beta_1$ and subsequently $\alpha'_2 = -2\beta_1$ (see the general relation $\alpha'_1 + \alpha'_2 + \alpha'_3 = 0$ valid for any stacking in Note S2†); for ABA stacking, the top layer and bottom layer are also in the equivalent positions, and it has the same form of inter-layer bond vectors as AA′A stacking but different inter-layer bond polarizabilities, thereby giving $\alpha'_1 = \alpha'_3 = \beta_2$ and subsequently $\alpha'_2 = -2\beta_2$ (note that β_1 and β_2 are related to the inter-layer bond polarizabilities of AA′ and AB stackings, respectively); for ABC stacking, the layer–layer stacking assumes the same AB type as ABA stacking (*i.e.*, BC stacking equivalent to BA), but layer 2 and layer 3 have different stacking directions and thus the opposite inter-layer bond directions compared to ABA stacking, thus yielding $\alpha'_1 = -\alpha'_3 = \beta_2$ and subsequently $\alpha'_2 = 0$; for AA′B′ and A′B′B stackings, the situation is more complicated due to a mixture of AA′ stacking and AB stacking, and we can derive $(\alpha'_1,\alpha'_2,\alpha'_3) = (\beta_1,-\beta_1 + \beta_2,-\beta_2)$ for AA′B′ stacking and $(\beta_2,-\beta_2 - \beta_1,\beta_1)$ for A′B′B stacking (more details in Note S2† and our previous theory work).[70] Although the polarizability derivatives show strong dependence on the stacking sequences, the frequencies and eigenvectors (*i.e.*, layer displacements) of inter-layer vibration modes are insensitive to the stacking patterns as demonstrated in the aforementioned experimental data. There are two inter-layer shear modes (S_1 and S_2) for the trilayer, and the normalized displacements of layer 1, layer 2 and layer 3 are $(\Delta x_1, \Delta x_2, \Delta x_3) = \frac{1}{\sqrt{2}}(1, 0, -1)$ for the lower-frequency S_1, and $\frac{1}{\sqrt{1.5}}(0.5, -1, 0.5)$ for the higher-frequency S_2, according to the linear chain model. Based on the formula $\Delta\alpha = \sum_i \alpha'_i \cdot \Delta x_i$ and $I \propto \frac{n+1}{\omega}|\Delta\alpha|^2$, we can obtain Raman intensities of the shear modes S_1 and S_2 for different stacking configurations in trilayer GaSe (detailed derivations in Note S2†):

$$\begin{array}{ll} I(\mathrm{AA'\,A}, S_1) = 0; & I(\mathrm{AA'\,A}, S_2) \propto 4.68|\beta_1|^2; \\ I(\mathrm{ABA}, S_1) = 0; & I(\mathrm{ABA}, S_2) \propto 4.68|\beta_2|^2; \\ I(\mathrm{ABC}, S_1) \propto 4.60|\beta_2|^2; & I(\mathrm{ABC}, S_2) = 0; \\ I(\mathrm{AA'\,B'}, S_1) \propto 1.15|\beta_1 + \beta_2|^2; & I(\mathrm{AA'\,B'}, S_2) \propto 1.17|\beta_1 - \beta_2|^2; \\ I(\mathrm{A'\,B'\,B}, S_1) \propto 1.15|\beta_1 - \beta_2|^2; & I(\mathrm{A'\,B'\,B}, S_2) \propto 1.17|\beta_1 + \beta_2|^2. \end{array} \quad (1)$$

From eqn (1) it is evident that for both ABA and AA′A stacking sequences, only the higher-frequency S_2 mode shows non-zero Raman intensity, corresponding to the experimental Raman spectrum of type 4 shown in Fig. 3a and also consistent with the DFT data shown in Fig. 4a. For ABC stacking, on the other hand, only the lower-frequency S_1 mode can be observed, consistent with the experimental Raman spectrum of type 2 shown in Fig. 3a and the DFT counterpart shown in Fig. 4a. Such opposite trends between ABA and ABC stacking sequences are directly related to the different polarizability derivatives of layer 2 and layer 3 stemming from the opposite stacking directions and inter-layer bond directions between layer 2 and layer 3, as discussed before. It is interesting to point out that I(ABA,S_2) ≈ I(ABC,S_1) according to eqn (1), in agreement with the experiment data of type 4 and type 2 shown in Fig. 3a and the DFT results shown in Fig. 4a.

For both AA′B′ and A′B′B stacking sequences, due to the mixture of two stacking types (AA′ and AB), it is expected that both S_1 and S_2 peaks can be detected. As the coefficients 1.15 and 1.17 in eqn (1) are about the same, the intensity ratio between S_1 and S_2 modes is roughly $r \approx \frac{|\beta_1 + \beta_2|^2}{|\beta_1 - \beta_2|^2}$ for AA′B′ stacking, while $r' \approx \frac{|\beta_1 - \beta_2|^2}{|\beta_1 + \beta_2|^2} \approx \frac{1}{r}$ for A′B′B stacking. We note that the system polarizability (or dielectric function) is complex, and has both real and imaginary parts due to the light absorption in experimental Raman scattering. Therefore, β_1 and β_2, parameters related to the inter-layer bond polarizabilities are complex as well. We can define $\beta_1 = |\beta_1|e^{i\phi_1}$ and $\beta_2 = |\beta_2|e^{i\phi_2}$, where ϕ_1 and ϕ_2 are their phase angles, respectively. Consequently, $r = \frac{|\beta_1|^2+|\beta_2|^2+2|\beta_1||\beta_2|\cos(\phi_1-\phi_2)}{|\beta_1|^2+|\beta_2|^2-2|\beta_1||\beta_2|\cos(\phi_1-\phi_2)}$, where the difference in the phase angle $\phi_1 - \phi_2$ affects the magnitude of r. For non-resonant Raman scattering where the incident laser photons do not excite electrons, ϕ_1 and ϕ_2 should be close to zero and $\phi_1 - \phi_2$ is typically between 0° and 90°. Consequently, we have $r > 1$, and thus $I(S_1) > I(S_2)$ for AA′B′ stacking while $I(S_1) < I(S_2)$ for A′B′B stacking. This is consistent with the DFT calculations of non-resonant Raman scattering in Fig. 4a, where $I(S_1) < I(S_2)$ for A′B′B stacking. However, when

the laser wavelength is near the energy of an electronic transition, ϕ_1 and ϕ_2 could change dramatically, leading to different intensity ratios between S_1 and S_2 modes. Therefore, there are some ambiguities in determining AA′B′ and A′B′B stacking sequences based on the Raman peak intensities of S_1 and S_2 alone.

The peak positions and the corresponding intensity ratio of peaks S_1 and S_2 from our calculations (Fig. 4a and eqn (1)) are compared with the experimental results shown in Fig. 3a to match the ultra-low-frequency Raman spectra with specific stacking sequences: type 1 to AA′B′ or A′B′B, type 2 to ABC, type 3 to A′B′B or AA′B′, and type 4 to ABA or AA′A. Only the type 2 Raman spectrum can be unambiguously identified as the ABC stacking sequence, whereas there are ambiguities for the other types.

In order to identify the stacking sequences, we performed HR-S/TEM analysis on trilayer samples. For these purposes the GaSe samples were exfoliated on PDMS and transferred to mono- or bi-layer graphene on the SiO_2/Si substrate to protect the samples from etchants during the transfer process to TEM grids. After the Raman spectra were collected, the samples were transferred onto TEM grids for HR-S/TEM analysis. We analyzed several areas of each sample in order to ascertain the repeatability. The stacking sequences are assigned by comparing the HR-S/TEM data with simulations shown in Fig. 5a–d. The simulated intensities along the red lines are shown below the simulated images. In the ABC stacking sequence, all the spots have the same intensity because each spot corresponds to 2 Ga atoms and 2 Se atoms, whereas the AA′B′, A′B′B and ABA stacking sequences have three different intensities for the spots (see Fig. S7 and Table S2†). On the other hand, the AA′A stacking sequence has an in-plane hexagonal structure without centered atoms, which makes it distinct from the other stacking sequences. First of all, the type 2 sample, which was identified as the ABC stacking sequence by comparing the Raman spectrum with the theoretical calculation, indeed shows an ABC-type HR-STEM image. The type 4 sample, which was classified as either the ABA or AA′A stacking sequences from the Raman spectrum and Raman calculation, cannot be the AA′A stacking sequence because there is a center spot in the hexagon. Therefore, we conclude that the type 4 sample corresponds to the ABA stacking sequence. The type 3 sample can be either AA′B′ or A′B′B stacking sequence as observed from Raman analysis. These two types have similar HR-S/TEM images because the atomic numbers of Ga and Se are not very different: the AA′B′ stacking sequence has a spot with 2 Se atoms whereas the A′B′B stacking sequence has a spot with 2 Ga atoms (see Fig. S7 and Table S2†). From the HR-S/TEM image, the intensities of the spots have the ratio of 1 : 1.3 : 2.7, whereas the expected ratios for AA′B′ or A′B′B stacking

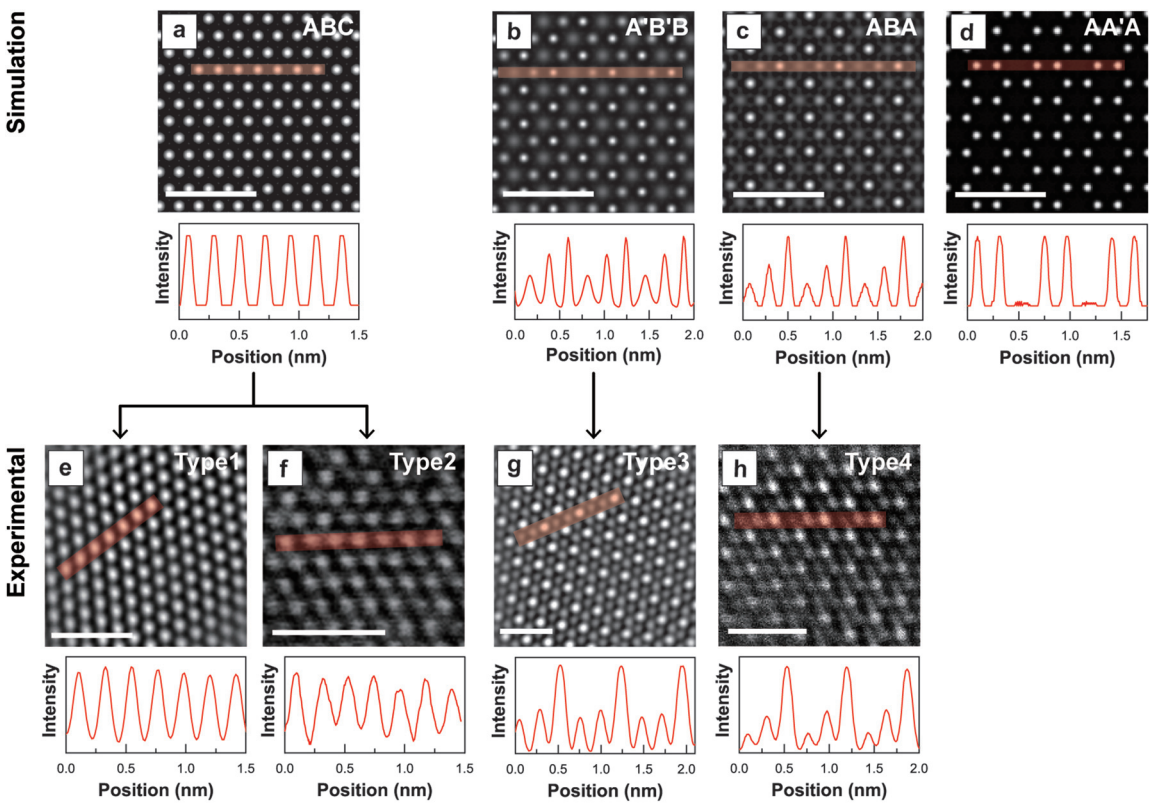

Fig. 5 HR-STEM and HR-TEM results from four different types of trilayer samples. (a–d) Simulated HR-TEM images of trilayer GaSe for the stacking sequences indicated. (e) Measured HR-TEM image and intensity line profile along the red line in the image for type 1 sample. (f–h) The HR-STEM images and intensity line profiles along the red lines in each high-resolution image for type 2, type 3, and type 4, respectively. The scale bar is 1 nm.

sequences are 1 : 1.51 : 1.98 and 1 : 1.65 : 2.18, respectively (see Table S2†). The experimental intensity ratio is slightly closer to the expected ratio for the A′B′B stacking sequence. Based on the analyses of the relative intensities of S_1 and S_2 in the Raman spectrum and the HR-S/TEM image we conclude that the type 3 sample is more likely to be the A′B′B stacking sequence. There is a possibility that the type 3 sample actually corresponds to the ABA stacking sequence (type 4 Raman spectrum), but the forbidden Raman peak at 9.6 cm^{-1} appears due to disorder or other effects that relax the selection rule. However, we found that there is a bilayer region with the AA′-type stacking in the surrounding area, which supports our assignment that this region is indeed the A′B′B stacking sequence. Finally, the identification of type 1 is more challenging: from Raman analysis, it was assigned to either AA′B′ or A′B′B stacking sequence. However, HR-TEM analysis indicates that it is the ABC stacking sequence although some disorder was observed in the surrounding region (see Fig. S8†). We interpret that this region is indeed the ABC stacking sequence, but the forbidden Raman peak of S_2 (16.6 cm^{-1}) appears due to the relaxation of the selection rule caused by the disorder because the laser spot for Raman measurements is much larger than the sampling area of the HR-S/TEM analysis.

We never found the AA′A stacking sequence in our HR-S/TEM measurements, although this stacking sequence (β-GaSe in bulk) has been reported in bulk GaSe studies.[53] Furthermore, in many ultra-low-frequency Raman spectra that we measured, we never encountered a spectrum with a different position for shear mode S_2 as expected from the AA′A stacking sequence according to our calculations (Fig. 4a). We suspect that this stacking sequence does not exfoliate as easily as the other stacking sequences or this stacking is unstable in few-layers or it could easily transit to other stacking sequences. The classification of stacking sequences is summarized in Table 1. Among many samples that we measured, the type 2 (ABC) and the type 4 (ABA) spectra were more frequently observed than the other types, which implies that the AB-type stacking is probably more stable and common than the AA′-type stacking. This is corroborated by our theoretical calculations: for the bilayer, the AB stacking is energetically more stable than the AA′ stacking by ~1.1 meV per unit cell; for the trilayer, the ABA, ABC, and A′B′B stacking patterns are more stable than the AA′A stacking by 2.3 meV per unit cell, 2.4 meV per unit cell, and 1.2 meV per unit cell, respectively. These trends do suggest that the AB stacking between two adjacent layers should be more common than the AA′ stacking.

Table 1 Assignment of stacking sequences of trilayer GaSe samples

Raman spectrum	Theory and HR-S/TEM
Type 1	Disordered ABC
Type 2	ABC
Type 3	A′B′B
Type 4	ABA

4. Conclusions

We investigated 2D layered GaSe by using polarized Raman spectroscopy as a function of the number of layers and the polarization angle. We found a blueshift of the high-frequency intra-layer $A'_1(1)$ modes as the number of layers increases whereas other high-frequency peak positions do not change much. More importantly, the low-frequency shear and breathing modes from inter-layer vibrations were observed, and they are more sensitive to the thickness and stacking. We can determine the number of layers using the peak positions of the low-frequency shear modes and the mode along with AFM. We found that the ultra-low-frequency spectra are very different even for the same thickness in the same flake. By comparing the ultra-low-frequency Raman spectra with theoretical calculations and HR-S/TEM measurements, we established the correlation between the ultra-low-frequency Raman spectra and the stacking sequences for trilayer GaSe. We further found that the AB-type stacking is more stable than the AA′-type stacking in GaSe. Our findings demonstrate that the inter-layer shear modes (frequencies and intensities) can be effective indicators of thickness and stacking in few-layer GaSe, the two key parameters governing the electronic and optical properties of 2D materials.

Author contributions

S.Y.L. prepared the samples and carried out the Raman measurements. T.T.H.N and S.C. provided the bulk crystal. L.L. and X.K. calculated theoretical Raman spectra and contributed to theoretical analysis. J.H.K. and Z.L. carried out S/TEM analysis. S.Y.L., J.-U.L., L.L., and H.C. interpreted the spectroscopic data.

Conflicts of interest

There are no conflicts to declare.

Acknowledgements

This work was supported by the National Research Foundation (NRF) grant funded by the Korean government (MSIT) (NRF-2014R1A4A1071686, 2018R1A2A2A05019598, 2019R1A2C3006189, 2019R1F1A1058473, and no. 2017R1A5A1014862, SRC program: vdWMRC center), by a grant IBS-R019-D1, and by a grant (no. 2013M3A6A5073173) from the Center for Advanced Soft Electronics under the Global Frontier Research Program of MSIT. A portion of this research (Raman scattering modeling) used resources available at the Center for Nanophase Materials Sciences, which is a US Department of Energy Office of Science User Facility. L. L. and X. K. acknowledge the work conducted at the Center for Nanophase Materials Sciences. S. Y. L. acknowledges support from the Hyundai Motor Chung Mong-Koo Foundation.

References

1 K. S. Novoselov, *Science*, 2004, **306**, 666–669.
2 K. F. Mak, C. Lee, J. Hone, J. Shan and T. F. Heinz, *Phys. Rev. Lett.*, 2010, **105**, 136805.
3 Q. H. Wang, K. Kalantar-Zadeh, A. Kis, J. N. Coleman and M. S. Strano, *Nat. Nanotechnol.*, 2012, **7**, 699–712.
4 Y. Zhang, T.-R. Chang, B. Zhou, Y.-T. Cui, H. Yan, Z. Liu, F. Schmitt, J. Lee, R. Moore, Y. Chen, H. Lin, H.-T. Jeng, S.-K. Mo, Z. Hussain, A. Bansil and Z.-X. Shen, *Nat. Nanotechnol.*, 2014, **9**, 111–115.
5 F. Xia, H. Wang, D. Xiao, M. Dubey and A. Ramasubramaniam, *Nat. Photonics*, 2014, **8**, 899–907.
6 K. F. Mak and J. Shan, *Nat. Photonics*, 2016, **10**, 216–226.
7 P. Hu, Z. Wen, L. Wang, P. Tan and K. Xiao, *ACS Nano*, 2012, **6**, 5988–5994.
8 P. Hu, L. Wang, M. Yoon, J. Zhang, W. Feng, X. Wang, Z. Wen, J. C. Idrobo, Y. Miyamoto, D. B. Geohegan and K. Xiao, *Nano Lett.*, 2013, **13**, 1649–1654.
9 S. R. Tamalampudi, Y.-Y. Lu, R. Kumar, U. R. Sankar, C.-D. Liao, K. Moorthy, B. C.-H. Cheng, F. C. Chou and Y.-T. Chen, *Nano Lett.*, 2014, **14**, 2800–2806.
10 E. Aulich, J. L. Brebner and E. Mooser, *Phys. Status Solidi*, 1969, **31**, 129–131.
11 E. Mooser and M. Schlüter, *Nuovo Cimento*, 1973, **18**, 164–208.
12 N. C. Fernelius, *Prog. Cryst. Growth Charact. Mater.*, 1994, **28**, 275–353.
13 L. Karvonen, A. Säynätjoki, S. Mehravar, R. D. Rodriguez, S. Hartmann, D. R. T. Zahn, S. Honkanen, R. A. Norwood, N. Peyghambarian, K. Kieu, H. Lipsanen and J. Riikonen, *Sci. Rep.*, 2015, **5**, 10334.
14 D. V. Rybkovskiy, N. R. Arutyunyan, A. S. Orekhov, I. A. Gromchenko, I. V. Vorobiev, A. V. Osadchy, E. Y. Salaev, T. K. Baykara, K. R. Allakhverdiev and E. D. Obraztsova, *Phys. Rev. B: Condens. Matter Mater. Phys.*, 2011, **84**, 085314.
15 Y. Ma, Y. Dai, M. Guo, L. Yu and B. Huang, *Phys. Chem. Chem. Phys.*, 2013, **15**, 7098–7105.
16 J. F. Sánchez-Royo, G. Muñoz-Matutano, M. Brotons-Gisbert, J. P. Martínez-Pastor, A. Segura, A. Cantarero, R. Mata, J. Canet-Ferrer, G. Tobias, E. Canadell, J. Marqués-Hueso and B. D. Gerardot, *Nano Res.*, 2014, **7**, 1556–1568.
17 X. Li, M.-W. Lin, A. A. Puretzky, J. C. Idrobo, C. Ma, M. Chi, M. Yoon, C. M. Rouleau, I. I. Kravchenko, D. B. Geohegan and K. Xiao, *Sci. Rep.*, 2015, **4**, 5497.
18 M.-W. Chen, H. Kim, D. Ovchinnikov, A. Kuc, T. Heine, O. Renault and A. Kis, *npj 2D Mater. Appl.*, 2018, **2**, 2.
19 C. S. Jung, F. Shojaei, K. Park, J. Y. Oh, H. S. Im, D. M. Jang, J. Park and H. S. Kang, *ACS Nano*, 2015, **9**, 9585–9593.
20 X. Li, M.-W. Lin, J. Lin, B. Huang, A. A. Puretzky, C. Ma, K. Wang, W. Zhou, S. T. Pantelides, M. Chi, I. Kravchenko, J. Fowlkes, C. M. Rouleau, D. B. Geohegan and K. Xiao, *Sci. Adv.*, 2016, **2**, e1501882.
21 M. Aoki and H. Amawashi, *Solid State Commun.*, 2007, **142**, 123–127.
22 H. Luo, W. Xie, J. Tao, H. Inoue, A. Gyenis, J. W. Krizan, A. Yazdani, Y. Zhu and R. J. Cava, *Proc. Natl. Acad. Sci. U. S. A.*, 2015, **112**, E1174–E1180.
23 G. Constantinescu, A. Kuc and T. Heine, *Phys. Rev. Lett.*, 2013, **111**, 036104.
24 W. Bao, L. Jing, J. Velasco, Y. Lee, G. Liu, D. Tran, B. Standley, M. Aykol, S. B. Cronin, D. Smirnov, M. Koshino, E. McCann, M. Bockrath and C. N. Lau, *Nat. Phys.*, 2011, **7**, 948–952.
25 C. H. Lui, Z. Li, K. F. Mak, E. Cappelluti and T. F. Heinz, *Nat. Phys.*, 2011, **7**, 944–947.
26 K. Zou, F. Zhang, C. Clapp, A. H. MacDonald and J. Zhu, *Nano Lett.*, 2013, **13**, 369–373.
27 C. H. Lui, Z. Li, Z. Chen, P. V. Klimov, L. E. Brus and T. F. Heinz, *Nano Lett.*, 2011, **11**, 164–169.
28 C. Cong, T. Yu, K. Sato, J. Shang, R. Saito, G. F. Dresselhaus and M. S. Dresselhaus, *ACS Nano*, 2011, **5**, 8760–8768.
29 C. H. Lui, L. M. Malard, S. Kim, G. Lantz, F. E. Laverge, R. Saito and T. F. Heinz, *Nano Lett.*, 2012, **12**, 5539–5544.
30 T. A. Nguyen, J.-U. Lee, D. Yoon and H. Cheong, *Sci. Rep.*, 2015, **4**, 4630.
31 X. Lu, M. I. B. Utama, J. Lin, X. Luo, Y. Zhao, J. Zhang, S. T. Pantelides, W. Zhou, S. Y. Quek and Q. Xiong, *Adv. Mater.*, 2015, **27**, 4502–4508.
32 J.-U. Lee, K. Kim, S. Han, G. H. Ryu, Z. Lee and H. Cheong, *ACS Nano*, 2016, **10**, 1948–1953.
33 W. Na, K. Kim, J.-U. Lee and H. Cheong, *2D Mater.*, 2018, **6**, 015004.
34 A. Kuhn, A. Chevy and R. Chevalier, *Phys. Status Solidi A*, 1975, **31**, 469–475.
35 Z. S. Basinski, D. B. Dove and E. Mooser, *J. Appl. Phys.*, 1963, **34**, 469–478.
36 J. C. J. M. Terhell and R. M. A. Lieth, *J. Cryst. Growth*, 1972, **16**, 54–58.
37 J. C. Irwin, R. M. Hoff, B. P. Clayman and R. A. Bromley, *Solid State Commun.*, 1973, **13**, 1531–1536.
38 M. Hayek, O. Brafman and R. M. A. Lieth, *Phys. Rev. B: Solid State*, 1973, **8**, 2772–2779.
39 H. Yoshida, S. Nakashima and A. Mitsuishi, *Phys. Status Solidi B*, 1973, **59**, 655–666.
40 E. Finkman and A. Rizzo, *Solid State Commun.*, 1974, **15**, 1841–1845.
41 S. Jandl and J. L. Brebner, *Can. J. Phys.*, 1974, **52**, 2454–2458.
42 R. M. Hoff, J. C. Irwin and R. M. A. Lieth, *Can. J. Phys.*, 1975, **53**, 1606–1614.
43 A. Polian, K. Kunc and A. Kuhn, *Solid State Commun.*, 1976, **19**, 1079–1082.
44 L. G. A. Gouskov and J. Camassel, *Prog. Cryst. Growth Charact.*, 1982, **5**, 323–413.
45 G. Kresse and J. Furthmüller, *Comput. Mater. Sci.*, 1996, **6**, 15–50.
46 H. J. Monkhorst and J. D. Pack, *Phys. Rev. B: Solid State*, 1976, **13**, 5188–5192.
47 L. Liang and V. Meunier, *Nanoscale*, 2014, **6**, 5394–5401.

48 A. A. Puretzky, L. Liang, X. Li, K. Xiao, B. G. Sumpter, V. Meunier and D. B. Geohegan, *ACS Nano*, 2016, **10**, 2736–2744.
49 K. Parlinski, Z. Li and Y. Kawazoe, *Phys. Rev. Lett.*, 1997, **78**, 4063–4066.
50 J. C. J. M. Terhell and R. M. A. Lieth, *Phys. Status Solidi A*, 1971, **5**, 719–724.
51 U. K. Gautam, S. R. C. Vivekchand, A. Govindaraj and C. N. R. Rao, *Chem. Commun.*, 2005, 3995.
52 D. J. Terry, V. Zólyomi, M. Hamer, A. V. Tyurnina, D. G. Hopkinson, A. M. Rakowski, S. J. Magorrian, N. Clark, Y. M. Andreev, O. Kazakova, K. Novoselov, S. J. Haigh, V. I. Fal'ko and R. Gorbachev, *2D Mater.*, 2018, **5**, 041009.
53 T. J. Wieting and J. L. Verble, *Phys. Rev. B: Solid State*, 1972, **5**, 1473–1479.
54 M. Yamamoto, S. T. Wang, M. Ni, Y. F. Lin, S. L. Li, S. Aikawa, W.-B. Jian, K. Ueno, K. Wakabayashi and K. Tsukagoshi, *ACS Nano*, 2014, **8**, 3895–3903.
55 N. N. Berchenko, O. A. Balitskii, R. V. Lutsiv, V. P. Savchyn and V. I. Vasyltsiv, *Mater. Chem. Phys.*, 1997, **51**, 125–129.
56 O. A. Balitskii and V. Savchyn, *Mater. Sci. Semicond. Process.*, 2004, **7**, 55–58.
57 T. E. Beechem, B. M. Kowalski, M. T. Brumbach, A. E. McDonald, C. D. Spataru, S. W. Howell, T. Ohta, J. A. Pask and N. G. Kalugin, *Appl. Phys. Lett.*, 2015, **107**, 173103.
58 A. Bergeron, J. Ibrahim, R. Leonelli and S. Francoeur, *Appl. Phys. Lett.*, 2017, **110**, 241901.
59 R. J. Nemanich, S. A. Solin and R. M. Martin, *Phys. Rev. B: Condens. Matter Mater. Phys.*, 1981, **23**, 6348–6356.
60 Y. Zhao, X. Luo, H. Li, J. Zhang, P. T. Araujo, C. K. Gan, J. Wu, H. Zhang, S. Y. Quek, M. S. Dresselhaus and Q. Xiong, *Nano Lett.*, 2013, **13**, 1007–1015.
61 X. Luo, X. Lu, C. Cong, T. Yu, Q. Xiong and S. Y. Quek, *Sci. Rep.*, 2015, **5**, 14565.
62 X.-F. Qiao, J.-B. Wu, L. Zhou, J. Qiao, W. Shi, T. Chen, X. Zhang, J. Zhang, W. Ji and P.-H. Tan, *Nanoscale*, 2016, **8**, 8324–8332.
63 L. Liang, J. Zhang, B. G. Sumpter, Q. H. Tan, P. H. Tan and V. Meunier, *ACS Nano*, 2017, **11**, 11777–11802.
64 N. S. Luo, P. Ruggerone and J. P. Toennies, *Phys. Rev. B: Condens. Matter Mater. Phys.*, 1996, **54**, 5051–5063.
65 P. H. Tan, W. P. Han, W. J. Zhao, Z. H. Wu, K. Chang, H. Wang, Y. F. Wang, N. Bonini, N. Marzari, N. Pugno, G. Savini, A. Lombardo and A. C. Ferrari, *Nat. Mater.*, 2012, **11**, 294–300.
66 K. H. Michel and B. Verberck, *Phys. Rev. B: Condens. Matter Mater. Phys.*, 2012, **85**, 094303.
67 R. Longuinhos and J. Ribeiro-Soares, *Phys. Chem. Chem. Phys.*, 2016, **18**, 25401–25408.
68 J.-B. Wu, Z. X. Hu, X. Zhang, W. P. Han, Y. Lu, W. Shi, X. F. Qiao, M. Ijiäs, S. Milana, W. Ji, A. C. Ferrari and P. H. Tan, *ACS Nano*, 2015, **9**, 7440–7449.
69 M.-L. Lin, T. Chen, W. Lu, Q.-H. Tan, P. Zhao, H.-T. Wang, Y. Xu and P.-H. Tan, *J. Raman Spectrosc.*, 2018, **49**, 46–53.
70 L. Liang, A. A. Puretzky, B. G. Sumpter and V. Meunier, *Nanoscale*, 2017, **9**, 15340–15355.
71 S. Huang, L. Liang, X. Ling, A. A. Puretzky, D. B. Geohegan, B. G. Sumpter, J. Kong, V. Meunier and M. S. Dresselhaus, *Nano Lett.*, 2016, **16**, 1435–1444.